To be published in Optics Letters:

Title:	Spectroscopic optical coherence refraction tomography
Authors:	Kevin Zhou,Ruobing Qian,Sina Farsiu,Joseph Izatt
Accepted:	05 March 20
Posted	06 March 20
DOI:	https://doi.org/10.1364/OL.389703

Spectroscopic optical coherence refraction tomography

KEVIN C. ZHOU[1,*], RUOBING QIAN[1], SINA FARSIU[1,2], AND JOSEPH A. IZATT[1,2]

[1] Department of Biomedical Engineering, Duke University, Durham, NC 27708
[2] Department of Ophthalmology, Duke University Medical Center, Durham, NC 27708
[*] Corresponding author: kevin.zhou@duke.edu

Compiled March 4, 2020

In optical coherence tomography (OCT), the axial resolution is often superior to the lateral resolution, which is sacrificed for long imaging depths. To address this anisotropy, we previously developed optical coherence refraction tomography (OCRT), which uses images from multiple angles to computationally reconstruct an image with isotropic resolution, given by the OCT axial resolution. On the other hand, spectroscopic OCT (SOCT), an extension of OCT, trades axial resolution for spectral resolution and hence often has superior lateral resolution. Here, we present spectroscopic OCRT (SOCRT), which uses SOCT images from multiple angles to reconstruct a spectroscopic image with isotropic spatial resolution limited by the OCT *lateral* resolution. We experimentally show that SOCRT can estimate bead size based on Mie theory at simultaneously high spectral and isotropic spatial resolution. We also applied SOCRT to a biological sample, achieving axial resolution enhancement limited by the lateral resolution.

http://dx.doi.org/10.1364/ao.XX.XXXXXX

Optical coherence tomography (OCT) is a cross-sectional imaging modality that uses a weakly focused beam for lateral discrimination and coherent ranging for depth discrimination. As such, the lateral resolution is typically greater than 10 µm in order to obtain an acceptable depth of focus in clinical applications such as ophthalmic imaging [1]. On the other hand, the axial resolution is determined independently by the source bandwidth and can be submicrometer [2]. To address this anisotropy in spatial resolution, we previously developed a technique called optical coherence refraction tomography (OCRT), which uses images acquired at multiple angles to computationally reconstruct a high-resolution image with isotropic resolution limited by the axial resolution of the original OCT system [3].

While in conventional OCT the axial resolution is typically superior to the lateral resolution, the reverse is often the case in spectroscopic OCT (SOCT) [4, 5], a functional extension of OCT that obtains depth-resolved, wavelength-dependent attenuation due to sample-induced absorption and scattering. SOCT has seen a variety of applications, such as assessing hemoglobin oxygenation [6–8], evaluating tissue burn severity [9], differentiating blood cell types [10], and detecting lipid [11]. However, because SOCT uses time-frequency analysis (e.g., short-time Fourier transform (STFT) or wavelet-based approaches) of OCT interferograms, there is an inverse relationship between the axial and spectral resolution. To address this tradeoff, previously the dual window (DW) method was reported [12]. However, it has been shown that DW can exhibit distorted spectra, compared to conventional STFTs, and does not fully avoid the tradeoff [13].

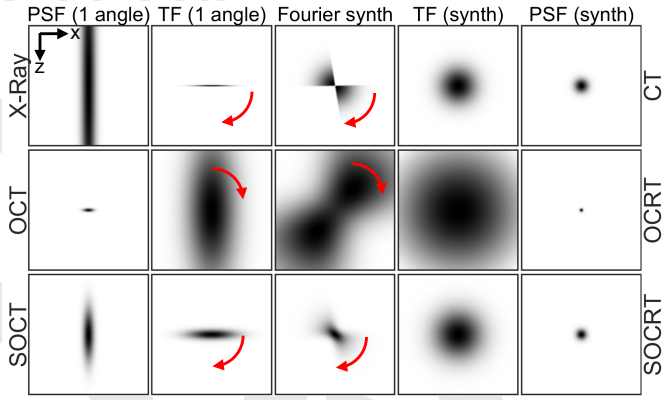

Fig. 1. CT, OCRT, and SOCRT (this work) are Fourier synthesis techniques. X-ray imaging and SOCT have superior x to z resolution, while OCT has superior z to x resolution. Upon multiangle reconstruction, the Fourier support of their transfer functions (TFs) becomes isotropic, conferring high spatial resolution given by the original x or z resolution, whichever is better. In our experiments, the OCT and SOCT axial/lateral resolutions were approximately 2.5/8.5 µm and 21-43 µm/8.5 µm, respectively, and thus the synthesized OCRT and SOCRT isotropic resolutions were 2.5 µm and 8.5 µm, respectively.

Here, we present spectroscopic OCRT (SOCRT), an extension of OCRT that uses angular diversity to improve the axial resolution to match the superior lateral resolution of SOCT, conferring an isotropic spatial resolution. As such, the spatial resolution is no longer constrained by the choice of the STFT window.

As SOCRT and OCRT are Fourier synthesis techniques, we compare them to X-ray computed tomography (CT) as a limiting case (Fig. 1). In CT, the resolution of a single projection is high

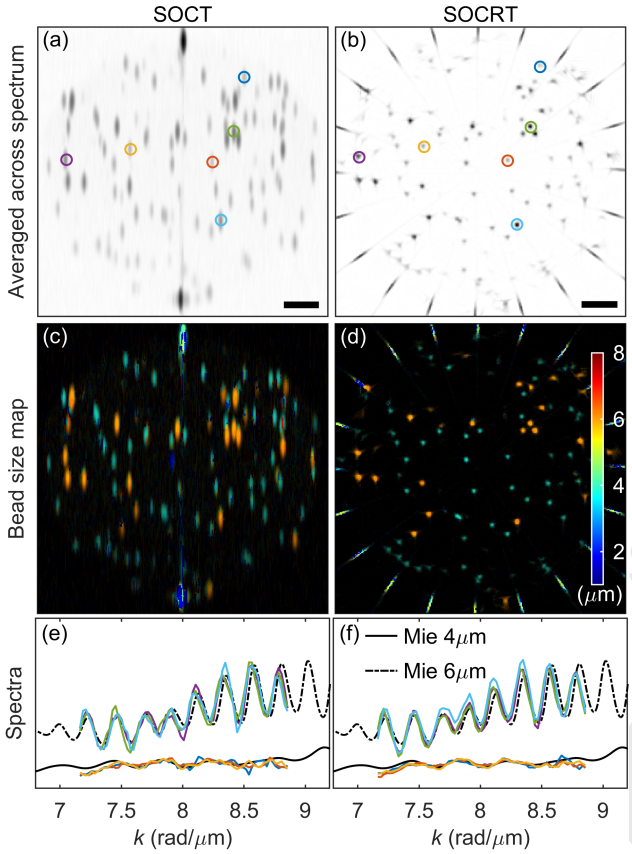

Fig. 2. Conventional SOCT (a, c, e) and SOCRT (b, d, f) of 4- and 6-μm polystyrene beads embedded in agarose. (a) and (b) are the SOCT B-scan from a single angle and the SOCRT reconstruction, respectively, both of which are averaged across the spectral dimension. (c) and (d) are the SOCT B-scans and SOCRT reconstruction, respectively, color-coded by bead size, based on fitting to Mie theory predictions. (e) and (f) show the bead spectra after fitting, color-coded according to the markers in (a) and (b), respectively. The same beads are selected in both the SOCT and SOCRT images for direct comparison. The spectra are consistent with Mie scattering theory for 4 μm and 6 μm, shown as the black and dashed black lines, respectively. The spoke artifacts in (b) and (d) are due to specular reflections from the glass tube surface. Scale bars, 100 μm.

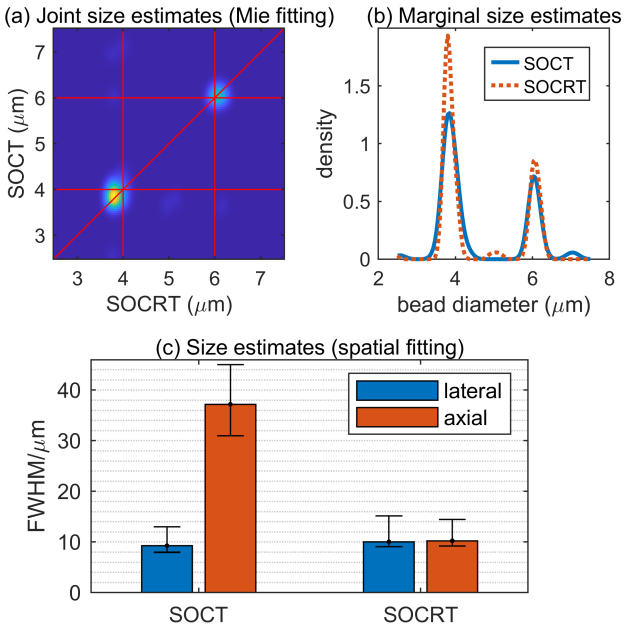

Fig. 3. Bead size quantification of results in Fig. 2. (a), (b) are, respectively, kernel density estimates of the joint and marginal distributions (i.e., the two 1D distributions obtained from integration across the rows and columns of the joint distribution) of the bead size estimates by SOCT and SOCRT via fitting to Mie theory, which are consistent with each other. The horizontal and vertical lines in (a) indicate the expected sizes, and the diagonal line indicates agreement between the two methods. (c) shows the distribution of bead widths (FWHM) based on 2D Gaussian fitting. The bar heights are medians, with 90% coverage intervals after removing poor fits.

in one dimension (x) and zero in the projection dimension (z), meaning that the point-spread function (PSF) is infinitely wide in z and the transfer function (TF) is zero in the z spatial frequency dimension. Rotating the sample or the setup effectively rotates the PSF and TF to cover more of the frequency space, approaching synthetic isotropic coverage as angular coverage approaches 180°. This Fourier synthesis can be achieved using the backprojection algorithm, in which a filter is applied to each projection prior to backprojection (i.e., filtered backprojection (FBP)) to counter the low-frequency bias.

For OCRT [3], the OCT lateral resolution is not zero, but still inferior to the axial resolution. Thus, the TF has high frequency support in the z direction, and some frequency support in the lateral direction. As with CT, acquisition of images from multiple angles followed by FBP renders isotropic coverage in Fourier space, and therefore isotropic resolution given by the original OCT axial width. As there is already some lateral frequency support, fewer angles are necessary than in CT.

For SOCRT, as the axial resolution of SOCT is sacrificed for the spectral resolution, the lateral resolution is often superior to the axial resolution. Therefore, the TF is wider in the lateral than axial dimension. Thus, multiangle acquisition and FBP confer isotropic spatial resolution consistent with the original SOCT lateral resolution and is unaffected by spectroscopic processing.

One crucial difference between CT and (S)OCRT is that while X-rays travel through essentially straight lines in biological tissue, light at visible and near-infrared wavelengths experiences spatially varying refractive index (RI) distributions, causing refraction and optical delay as a function of position and angle. Thus, the multiangle B-scans are in general distorted and not superimposable. To overcome this issue, we dewarp the individual A-scans of the B-scans according to the ray equation, which specifies a ray trajectory given its initial position and direction, and a RI distribution. In particular, we iteratively optimize the RI according to a joint intensity-based registration metric among all multiangle B-scans. Once the RI map is inferred, we deform the B-scans according to the propagated rays and then apply FBP to synthesize the isotropic, high-resolution image. Optionally, the FBP filter may be optimized at the end. A detailed description of the joint RI map inference, B-scan registration, and dewarping for OCRT is described in our previous publication [3].

SOCRT extends OCRT, sharing the registration and RI in-

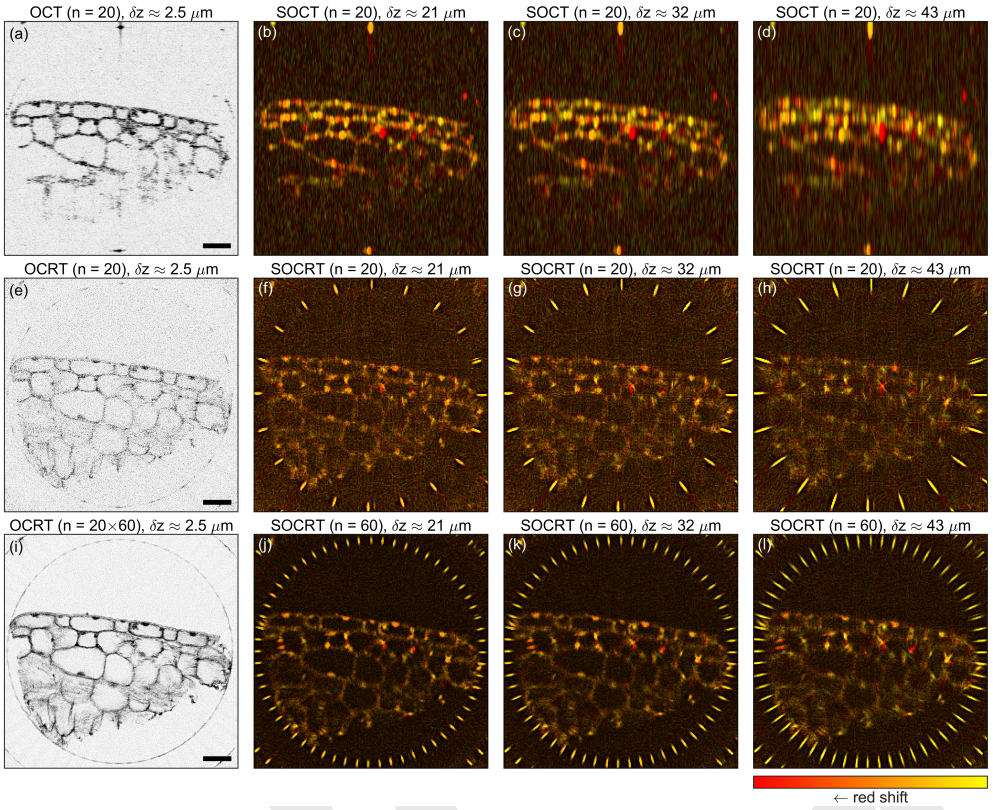

Fig. 4. SOCRT enhances the axial resolution of SOCT in an onion sample. (a) is a conventional OCT B-scan using the full source bandwidth (n=20 frames averaged). (e) and (i) are the corresponding OCRT reconstructions with improved axial resolution. (e) used unaveraged B-scans from 20 angles, while (i) used 20-averaged B-scans from 60 angles. (a) and (e) are histogram-matched to (f) (MATLAB function imhistmatch). (b)-(d) are SOCT images color-coded by center-of-mass shift of the spectra (20-averaged). The axial resolutions of these images, denoted by the column labels, were tuned using the width of the STFT sliding spectral window, with decreasing axial and therefore increasing spectral resolution from left to right. (f)-(h) are the corresponding unaveraged SOCRT reconstructions (using unaveraged B-scans from 20 angles), with improved axial resolution. (j)-(l) used 20-averaged B-scans from 60 angles. Scale bars, 100 μm.

ference steps based on multiangle B-scans, generated using a portion of or the full bandwidth. Next, we used a narrow sliding spectral window to generate the SOCT data stack (i.e., low-axial-resolution B-scans for each spectral position) for each angle, in other words a 4D data stack, $I_{SOCT}(x,z,k,\theta)$, whose dimensions are the two spatial dimensions, the spectral position of the sliding window, and the angle. Finally, using the optimized registration parameters (e.g., the RI map), we generated the OCRT reconstruction for each spectral position, the resulting stack of which constitutes the SOCRT data stack, $I_{SOCRT}(x,z,k)$.

Unlike in our previous publication [3], we did not perform filter optimization after registration, because the optimal filter not only would be different for the initial OCRT reconstruction using the full spectral bandwidth compared to the SOCRT reconstruction, but also may depend on the spectral position itself, which would make the optimization computationally expensive. Instead, noting that one common theme among the optimized filters was to remove a halo effect present due to excessive attenuation of frequency components near DC by the initial filter, we used a modified Ram-Lak filter, $H(f_x) = \sqrt{f_x^2 + \delta}$, where f_x is the lateral frequency and δ is a non-negative constant that prevents the filter from reaching 0 near DC. Note that when $\delta = 0$, the filter reduces to the conventional Ram-Lak ramp filter [14]. We also note that we applied this filter along the lateral dimension, the dimension of higher resolution for SOCT.

To demonstrate SOCRT experimentally, we used a commercial spectral-domain OCT system (Leica Bioptigen Envisu R4110 XHR SDOIS), with center wavelength of 820 nm and axial and lateral resolutions of ~2.5 μm and ~8.5 μm in tissue, respectively. To acquire multiangle data, we inserted all samples in this study into glass microcapillary tubes (Drummond Scientific, inner diameter of 0.8 mm), which were mounted on an inverted rotation stage and immersed in water. We acquired images evenly spaced over 360° (S)OCT images. The RI map for the OCRT optimization was initialized using the known RI values from calibration experiments prior to data collection.

We first imaged a phantom consisting of a sparse mixture of 4-μm and 6-μm polystyrene beads (n=1.58), embedded in 2% agarose inside a glass microcapillary tube (Fig. 2). To estimate the bead sizes, we analyzed the backscattered spectra, which for a spherical reflector has a dominant frequency component characteristic of the diameter of the bead, as predicted by Mie theory [15]. Each interferogram from each angle was processed using SOCT, specifically using STFTs with a sliding Gaussian window with a full width at half maximum (FWHM) of 0.048 μm^{-1} (5.2 nm at λ = 820 nm), giving a theoretical axial resolution of ~43 μm in water (Fig. 2(a)-(c)). We then applied SOCRT processing to enhance the axial resolution to match the system

lateral resolution of 8.5 µm for every spectral band (Fig. 2(d)-(f)). We found that registering B-scans derived from the full source bandwidth was difficult because the front and back surfaces of the beads were resolvable given the 2.5-µm axial resolution. To aid the registration, we reduced the axial resolution by windowing the spectrum such that the beads appeared as single reflectors. We also note that because in practice it was difficult to align the tube such that all the beads stayed in the same 8.5-µm thick plane throughout 360° of rotation, we digitally summed multiple B-scan slices in y (out-of-plane) across 54 µm before reconstructing. Furthermore, since we knew a priori that the RI map of this sample was very similar to the initialized value, during the initial OCRT registration stage we only optimized with respect to spatial shifts to account for residual experimental misalignment.

Fig. 2 compares the SOCT and SOCRT reconstruction results for this bead phantom. Although the SOCT images (Fig. 2(a), (c)) exhibit anisotropic spatial resolution, with higher lateral than axial resolution, SOCRT (Fig. 2(b), (d)) renders the resolution isotropic, matching the lateral resolution. In Fig. 2(a), (b), despite small differences in reflectivity of the 4- and 6-µm beads, they are difficult to differentiate. However, using spectroscopic information, the beads' sizes were estimated for SOCT and SOCRT (Fig. 2(c), (d)) based on fitting the spectra to Mie theory predictions [16] (assuming n=1.58). We accounted for the spectral envelope for each bead by first fitting to a linear combination of the spectra corresponding to the front and back inner surfaces of the glass tube wall, with a non-negativity constraint on the coefficients, and normalizing the spectra by the result. To further increase robustness of our Mie fitting procedure, we also accounted for any remaining linear trends. We have provided the MATLAB fitting code (Code 1) and the raw bead spectral data (Data File 1). The fidelity of the spectra are maintained in SOCRT with a similar spectral resolution to that of SOCT (Fig. 2(e), (f)), and in both cases the spectra are consistent not only with Mie theory [16], but also with each other, based on their respective bead size predictions (Fig. 3(a), (b)). Such consistency validates the spectroscopic capabilities of SOCRT, as particle sizing with SOCT has previously been demonstrated [17]. We also segmented the beads in Fig. 2(a), (d) and fit them to 2D Gaussians (Fig. 3(c)); for SOCT, we obtained median fit values of 9.3 and 37.2 µm for lateral and axial widths, respectively, and for SOCRT, we obtained 10.0 and 10.2 µm for lateral and axial widths. Thus, SOCRT renders the anisotropic spatial resolution of SOCT isotropic.

We further applied SOCRT to an onion sample (Fig. 4), which was also inserted into a glass microcapillary tube to assist with sample rotation. In addition to conventional OCT and OCRT processing (Fig. 4(a), (e), (i)), we chose three STFT spectral windows corresponding to theoretical axial resolutions of ∼21, ∼32, and ∼43 µm and performed SOCT (Fig. 4(b)-(d)) and SOCRT (Fig. 4(f)-(h) and (j)-(l)) processing. Fig. 4(f)-(h) show unaveraged reconstructions, using the same number of B-scans as in (b)-(d) for fair comparison. It is clear that regardless of the degree to which the SOCT axial resolution was reduced via the chosen STFT window width, SOCRT was able to enhance the axial resolution according to the original OCT lateral resolution.

In summary, we have presented SOCRT as an extension of OCRT to incorporate spectral information without the same tradeoff between the spectral and axial resolution characteristic of conventional SOCT. While in conventional OCT the axial is typically superior to the lateral resolution, in SOCT the reverse is often the case as a result of time-frequency analysis. Hence, this work may be thought of as a generalization of OCRT to a technique that renders the spatial resolution of anisotropic imaging modalities isotropic, given by the dimension with the highest resolution.

We note some limitations of this proof-of-concept study. As with our previous study [3], insertion of samples into glass tubes was only to aid in sample rotation and is not a requirement of (S)OCRT. For example, angular beam scanning would not only alleviate this problem, but also more readily extend this work to 3D by allowing 2D angular scanning. Another limitation is that our OCT source spectrum only covered near-infrared wavelengths, where biological molecules or pigments with strong absorptive features are lacking. Thus, future work includes applying SOCRT to visible-light SOCT [6, 18] and nonlinear-optics-based SOCT [19] in order to gain access to a wider array of chromophores, such as hemoglobin, chlorophyll, and lipids. Using such SOCT systems, we can exploit the speckle reduction of OCRT [3] in SOCRT, which averages away the angle-dependent structural features that would otherwise generate high-contrast speckle that may dominate the absorptive features, particularly in densely scattering tissue samples. Thus, SOCRT retains the angle-independent spectral features, which includes absorptive features and symmetric scattering structures (e.g., spherical nuclei).

Funding. National Science Foundation (NSF) (DGF-1106401, CBET-1902904).

Disclosures. All authors are inventors on a pending patent related to this work.

REFERENCES

1. A. C. Tan, G. S. Tan, A. K. Denniston, P. A. Keane, M. Ang, D. Milea, U. Chakravarthy, and C. M. G. Cheung, Eye **32**, 262 (2018).
2. B. Povazay, K. Bizheva, A. Unterhuber, B. Hermann, H. Sattmann, A. Fercher, W. Drexler, A. Apolonski, W. Wadsworth, J. Knight *et al.*, Opt. Lett. **27**, 1800 (2002).
3. K. C. Zhou, R. Qian, S. Degan, S. Farsiu, and J. A. Izatt, Nat. Photonics pp. 1–9 (2019).
4. U. Morgner, W. Drexler, F. Kärtner, X. Li, C. Pitris, E. Ippen, and J. Fujimoto, Opt. Lett. **25**, 111 (2000).
5. R. Leitgeb, M. Wojtkowski, A. Kowalczyk, C. Hitzenberger, M. Sticker, and A. Fercher, Opt. Lett. **25**, 820 (2000).
6. F. E. Robles, C. Wilson, G. Grant, and A. Wax, Nat. Photonics **5**, 744 (2011).
7. J. Yi, Q. Wei, W. Liu, V. Backman, and H. F. Zhang, Opt. Lett. **38**, 1796 (2013).
8. S. Pi, A. Camino, W. Cepurna, X. Wei, M. Zhang, D. Huang, J. Morrison, and Y. Jia, Biomed. Opt. Express **9**, 2056 (2018).
9. Y. Zhao, J. R. Maher, J. Kim, M. A. Selim, H. Levinson, and A. Wax, Biomed. Opt. Express **6**, 3339 (2015).
10. R. Qian, W.-f. Huang, R. P. McNabb, K. C. Zhou, Q. H. Liu, A. N. Kuo, and J. A. Izatt, Biomed. Opt. Express **10**, 3281 (2019).
11. C. P. Fleming, J. Eckert, E. F. Halpern, J. A. Gardecki, and G. J. Tearney, Biomed. Opt. Express **4**, 1269 (2013).
12. F. Robles, R. N. Graf, and A. Wax, Opt. Express **17**, 6799 (2009).
13. N. Bosschaart, T. G. van Leeuwen, M. C. Aalders, and D. J. Faber, Biomed. Opt. Express **4**, 2570 (2013).
14. L. A. Shepp and B. F. Logan, IEEE Trans. Nucl. Sci. **21**, 21 (1974).
15. C. Xu, P. S. Carney, and S. A. Boppart, Opt. Express **13**, 5450 (2005).
16. P. Laven, "Mieplot," http://www.philiplaven.com/mieplot.htm (2019).
17. F. E. Robles and A. Wax, Opt. Lett. **35**, 360 (2010).
18. X. Shu, L. J. Beckmann, and H. F. Zhang, J. Biomed. Opt. **22**, 121707 (2017).
19. F. E. Robles, K. C. Zhou, M. C. Fischer, and W. S. Warren, Optica. **4**, 243 (2017).

FULL REFERENCES

1. A. C. Tan, G. S. Tan, A. K. Denniston, P. A. Keane, M. Ang, D. Milea, U. Chakravarthy, and C. M. G. Cheung, "An overview of the clinical applications of optical coherence tomography angiography," Eye. **32**, 262 (2018).
2. B. Povazay, K. Bizheva, A. Unterhuber, B. Hermann, H. Sattmann, A. Fercher, W. Drexler, A. Apolonski, W. Wadsworth, J. Knight *et al.*, "Submicrometer axial resolution optical coherence tomography," Opt. Lett. **27**, 1800–1802 (2002).
3. K. C. Zhou, R. Qian, S. Degan, S. Farsiu, and J. A. Izatt, "Optical coherence refraction tomography," Nat. Photonics pp. 1–9 (2019).
4. U. Morgner, W. Drexler, F. Kärtner, X. Li, C. Pitris, E. Ippen, and J. Fujimoto, "Spectroscopic optical coherence tomography," Opt. Lett. **25**, 111–113 (2000).
5. R. Leitgeb, M. Wojtkowski, A. Kowalczyk, C. Hitzenberger, M. Sticker, and A. Fercher, "Spectral measurement of absorption by spectroscopic frequency-domain optical coherence tomography," Opt. Lett. **25**, 820–822 (2000).
6. F. E. Robles, C. Wilson, G. Grant, and A. Wax, "Molecular imaging true-colour spectroscopic optical coherence tomography," Nat. Photonics **5**, 744 (2011).
7. J. Yi, Q. Wei, W. Liu, V. Backman, and H. F. Zhang, "Visible-light optical coherence tomography for retinal oximetry," Opt. Lett. **38**, 1796–1798 (2013).
8. S. Pi, A. Camino, W. Cepurna, X. Wei, M. Zhang, D. Huang, J. Morrison, and Y. Jia, "Automated spectroscopic retinal oximetry with visible-light optical coherence tomography," Biomed. Opt. Express **9**, 2056–2067 (2018).
9. Y. Zhao, J. R. Maher, J. Kim, M. A. Selim, H. Levinson, and A. Wax, "Evaluation of burn severity in vivo in a mouse model using spectroscopic optical coherence tomography," Biomed. Opt. Express **6**, 3339–3345 (2015).
10. R. Qian, W.-f. Huang, R. P. McNabb, K. C. Zhou, Q. H. Liu, A. N. Kuo, and J. A. Izatt, "Ocular anterior chamber blood cell population differentiation using spectroscopic optical coherence tomography," Biomed. Opt. Express **10**, 3281–3300 (2019).
11. C. P. Fleming, J. Eckert, E. F. Halpern, J. A. Gardecki, and G. J. Tearney, "Depth resolved detection of lipid using spectroscopic optical coherence tomography," Biomed. Opt. Express **4**, 1269–1284 (2013).
12. F. Robles, R. N. Graf, and A. Wax, "Dual window method for processing spectroscopic optical coherence tomography signals with simultaneously high spectral and temporal resolution," Opt. Express **17**, 6799–6812 (2009).
13. N. Bosschaart, T. G. van Leeuwen, M. C. Aalders, and D. J. Faber, "Quantitative comparison of analysis methods for spectroscopic optical coherence tomography," Biomed. Opt. Express **4**, 2570–2584 (2013).
14. L. A. Shepp and B. F. Logan, "The fourier reconstruction of a head section," IEEE Trans. Nucl. Sci. **21**, 21–43 (1974).
15. C. Xu, P. S. Carney, and S. A. Boppart, "Wavelength-dependent scattering in spectroscopic optical coherence tomography," Opt. Express **13**, 5450–5462 (2005).
16. P. Laven, "Mieplot," http://www.philiplaven.com/mieplot.htm (2019).
17. F. E. Robles and A. Wax, "Measuring morphological features using light-scattering spectroscopy and fourier-domain low-coherence interferometry," Opt. Lett. **35**, 360–362 (2010).
18. X. Shu, L. J. Beckmann, and H. F. Zhang, "Visible-light optical coherence tomography: a review," J. Biomed. Opt. **22**, 121707 (2017).
19. F. E. Robles, K. C. Zhou, M. C. Fischer, and W. S. Warren, "Stimulated raman scattering spectroscopic optical coherence tomography," Optica. **4**, 243–246 (2017).